Supplemental Methods

Selection of genes targeted by WTA

Human protein-coding genes were determined based on the HUGO Gene Nomenclature Committee (HGNC) and designed according to the available RefSeq transcripts. Mouse protein-coding genes were determined based on Mouse Genome Informatics (MGI) and designed according to the available RefSeq transcripts. For mouse genes, we also considered the current status of genes in NCBI RefSeq and did not include those with poor status (Suppressed, Provisional, Model, or Inferred). Notably, 1,450 protein-coding genes that exist in the MGI database had no available mRNA transcripts in RefSeq at the time of design. By comparison, that number in human was only 31 and included a few genes that should have been characterized as loci and not protein-coding entities (ex. PCDHG@, TRD).

In order to provide the best sensitivity for lower-expressing transcripts, we elected to remove the top 10 most highly expressed genes in TCGA across tumor types from the human WTA (*ACTB*, *ACTG1*, *EEF1A1*, *EEF2*, *FTL*, *GAPDH*, *PSAP*, *RPL3*, *TPT1*, and *UBC*). A similar assessment was performed for mouse genes according to (Söllner et al. 2017) but as most of the genes identified were organ-specific, we opted to instead remove genes based on empirical data using our assay. Those genes were *Gm20594* and *Eef1a1*. *Eef1a1* is the mouse homolog of human *EEF1A1* we prospectively removed for the same rationale, and *Gm20594* is the human ortholog of *MTRNR2L7*, which has homology to mitochondrial rRNA and thus could yield very high counts. In both human and mouse WTA, mitochondrially-encoded transcripts were removed as they are also very highly expressed.

The final probe pool consists of 18,815 probes for human WTA and 20,175 probes for mouse WTA, including 139 negative control probes for human and 210 negative control probes for mouse. These probes target 19,505 and 21,596 annotated genes for human and mouse, of

which 19,128 and 21,040 are protein-coding respectively. Due to high homology in some gene families, 636 human probes and 656 mouse probes target more than one gene (Table S1).

Supplemental Figures

A

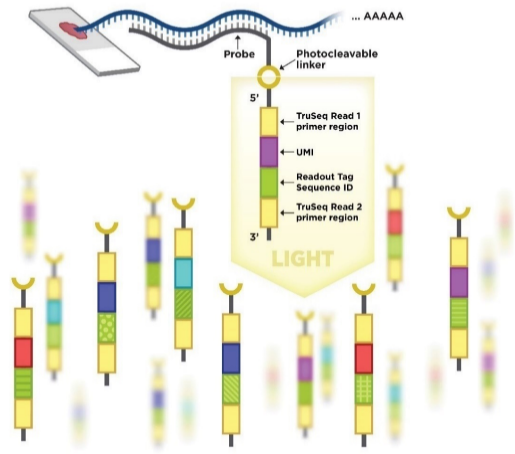

B

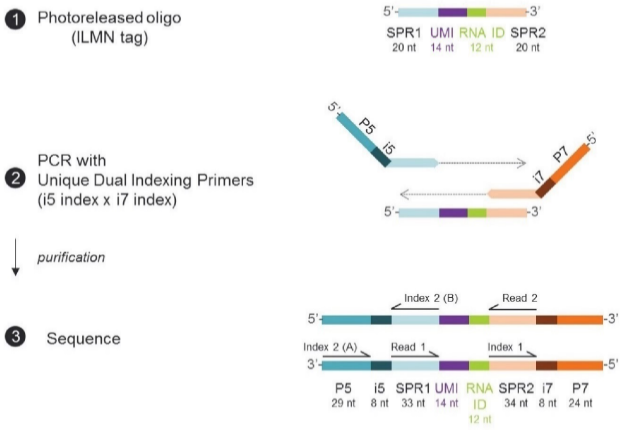

C

	Human WTA	Mouse WTA
Number of Genes Targeted	19505	21596
Number of Protein Coding Genes Targeted	19128	21040
Negative Control Probes	139	210
Total Number of Probes	18815	20175

Figure S1. WTA probe design. A. Schematic of WTA probes, with a sequence complementary to the target RNA, a UV-photocleavable linker, and an indexing tag sequence designed to be read out by high-throughput sequencing. The indexing tag sequence contains a UMI and a barcode designed to uniquely identify each probe. **B.** After release on the DSP instrument, the tag sequence is collected and amplified by PCR to add Illumina P5 and P7 sequences as well as i5 and i7 index sequences for sample demultiplexing after sequencing. **C.** Number of probes and genes targeted by the human and mouse WTAs.

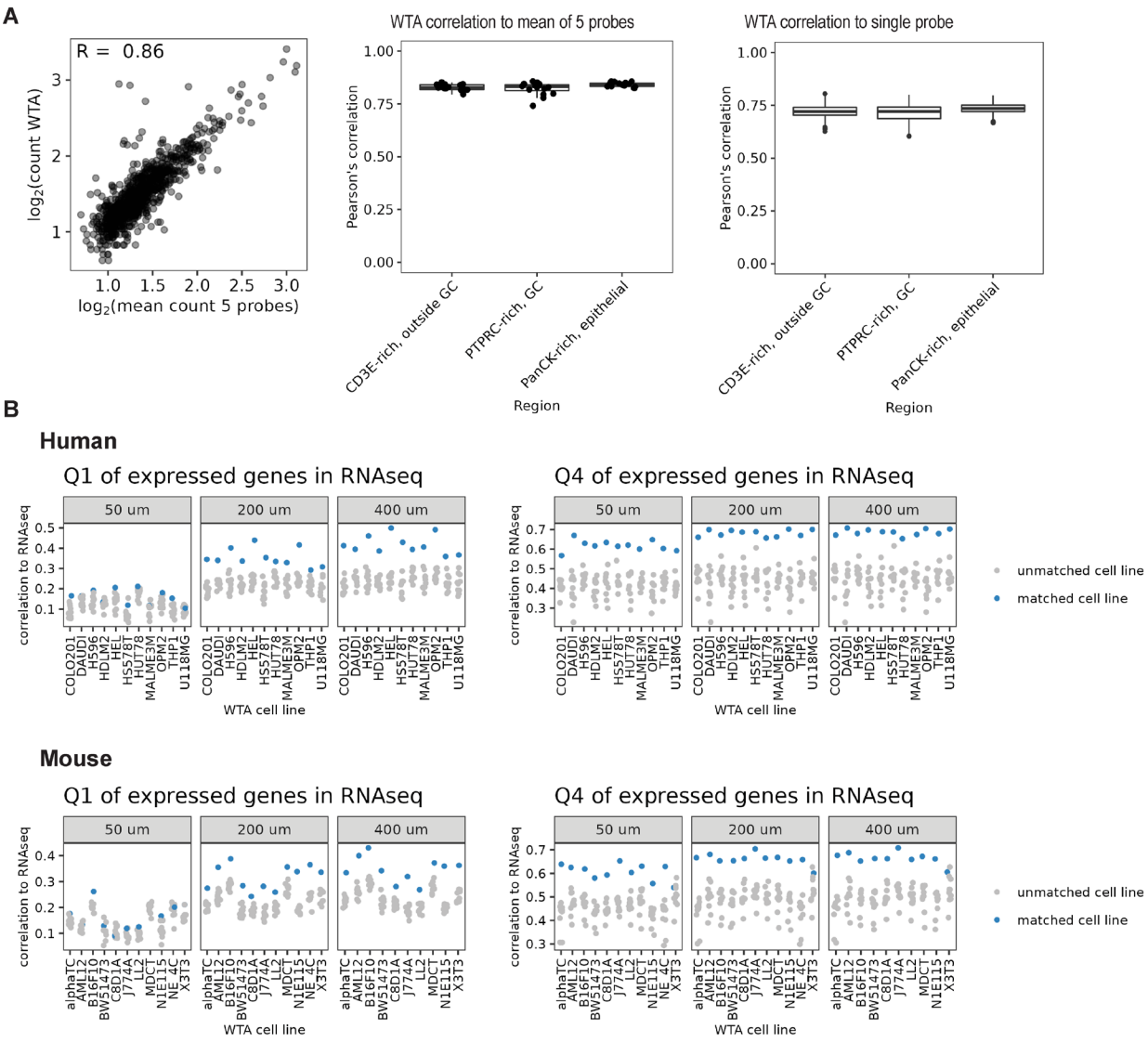

Figure S2. Correlation of WTA with other DSP panels and RNA-seq. A. Left: Scatterplot of WTA counts and the mean counts of an 1,812 gene panel with 5 probes per target for a representative matched AOI. Middle/Right: Boxplots of Pearson correlation coefficients between WTA and the mean count of 5 probes per target from the smaller panel, or 100 iterations of a randomly selected single probe. **B.** Spearman's correlation of WTA counts in each AOI compared to RNA-seq of each cell line profiled in this experiment using just the lowest quartile of expressed genes in the RNA-seq data (Q1), or the highest quartile of expressed genes (Q4). For each AOI, the matching cell line is shown in blue and all other cell lines in grey.

A

Human

Gene	H596	SUDHL4
MS4A1	0.07	690.15
PTPRC	0.09	166.38
CD27	0.19	181.92
CD48	0.43	218.28
CD79A	0.5	656.46
CXCL8	250.77	0.59
DKK1	258.89	0.4
C1R	350.12	0.47
ITGB4	358.74	0.93

Mouse

Gene	NE-4C	J774A.1
Ptprc	0	209.415
Aif1	0.106361	277.822
Itgam	0.139225	451.785
Rac2	0.27408	298.922
Sparc	114.693	0
Enpp2	116.856	0
Cd63	256.868	0
Epcam	306.483	0

B

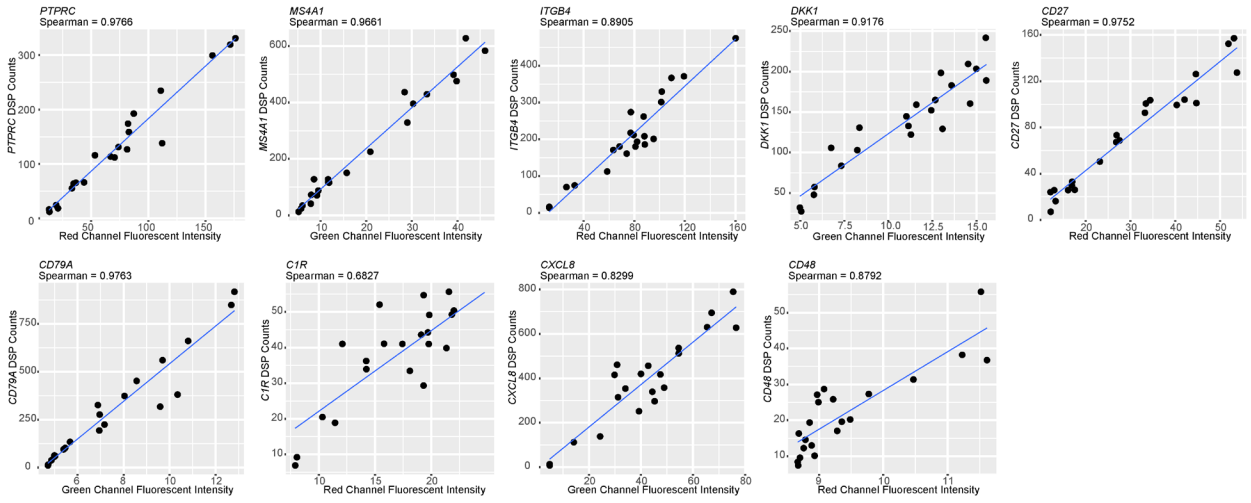

C

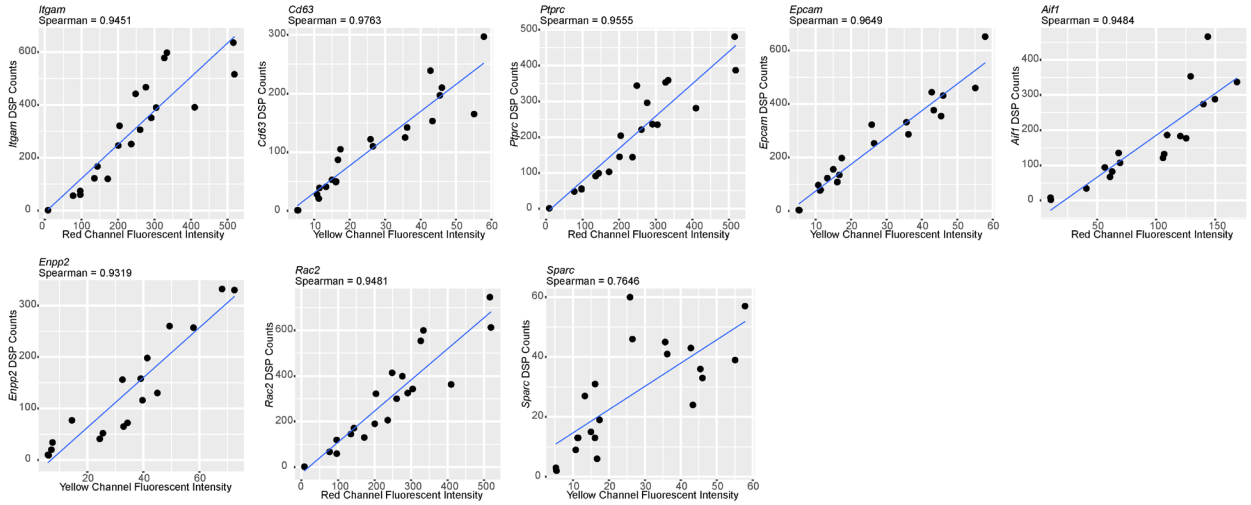

Figure S3. Correlation of WTA with RNA FISH in cell line titrations. A. Table showing RNA-seq TPM in each of the two cell lines in the titration for each gene tested by RNA FISH. Genes were selected for high (>100 TPM) in one cell line, and low (<1 TPM) expression in the other to create a gradient of gene expression across the titration. **B-C.** Scatterplots showing WTA counts

vs RNA FISH fluorescent intensity across the cell line titration for each gene tested in human (**B**) and mouse (**C**).

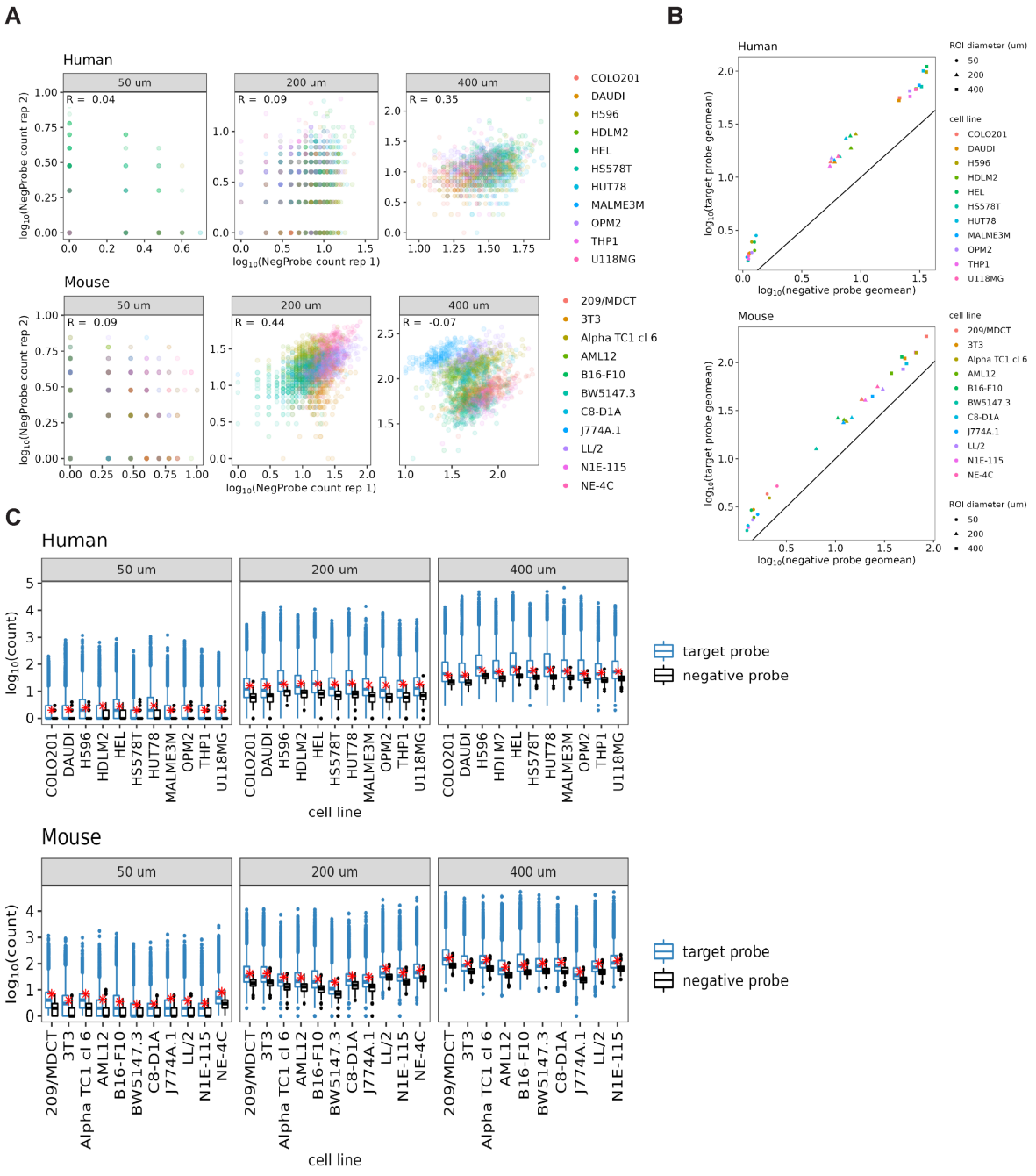

Figure S4. A. Log_{10} counts of all negative probes across replicate experiments in 11 FFPE human and mouse cell lines. Points are colored by cell line, and separated by AOI size. **B.** Relationship

between negative probe signal and target signal in each AOI in 11 FFPE human and mouse cell lines. The $\log_{10}$ geometric mean of negative probes is plotted on the x-axis, and the $\log_{10}$ geometric mean of target probes on the y-axis. Probes were filtered for outliers as described in the Methods. Line is y=x, and points are colored by cell line and shaped by AOI size. **C.** Boxplots showing target (in blue) and negative probe counts (in black) for all genes in 11 FFPE human and mouse cell pellets in 50, 200, and 400 µm-diameter circular AOIs. The red dot indicates 2 SD above the geometric mean of negative probe counts, the threshold used for calling a gene above background in this manuscript.

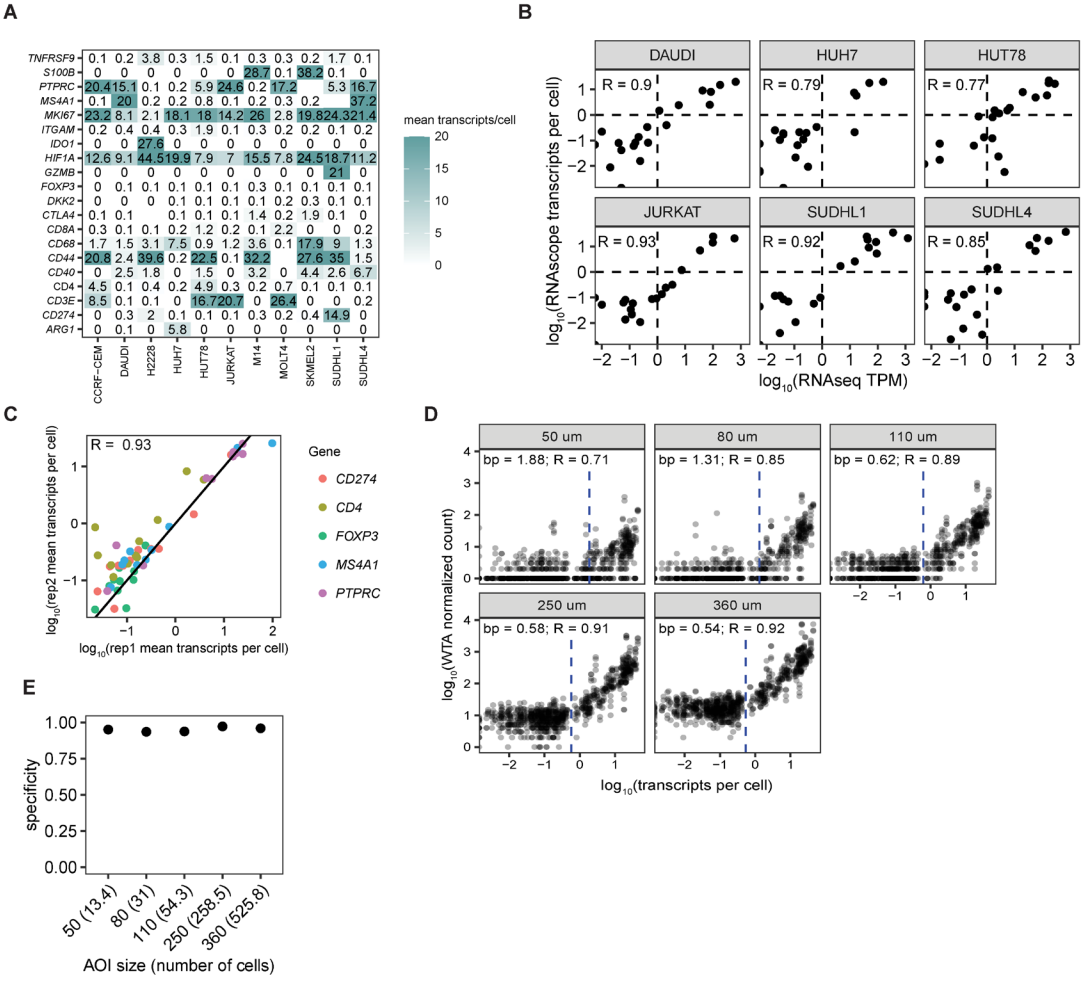

Figure S5. Sensitivity of WTA at different gene expression levels. A. Expression level of transcripts used in the RNAscope absolute transcript comparison experiment. Mean number of

transcripts per cell for each gene in each cell line is indicated. **B.** Scatterplots plotting $\log_{10}$(TPM) in the RNA-seq experiment on the x-axis, and $\log_{10}$(mean transcripts per cell) in the RNAscope experiment for each gene in each cell line tested in this experiment. Dashed lines indicate the threshold for calling a gene "expressed": 1 TPM in RNA-seq, and 1 transcript per cell in RNAscope. **C.** Replicability of RNAscope mean transcripts per cell for 5 genes run in duplicate experiments. **D.** Scatterplot of WTA counts on the y-axis vs mean transcripts per cell from RNAscope on the x-axis. Breakpoints at which WTA counts and RNAscope transcripts per cell become linearly correlated were calculated for each AOI size and are indicated by a dashed line. **E.** Specificity of human WTA compared to RNAscope in each AOI size, using RNAscope mean transcripts per cell ≥ 1 as the threshold for a true expressed gene.

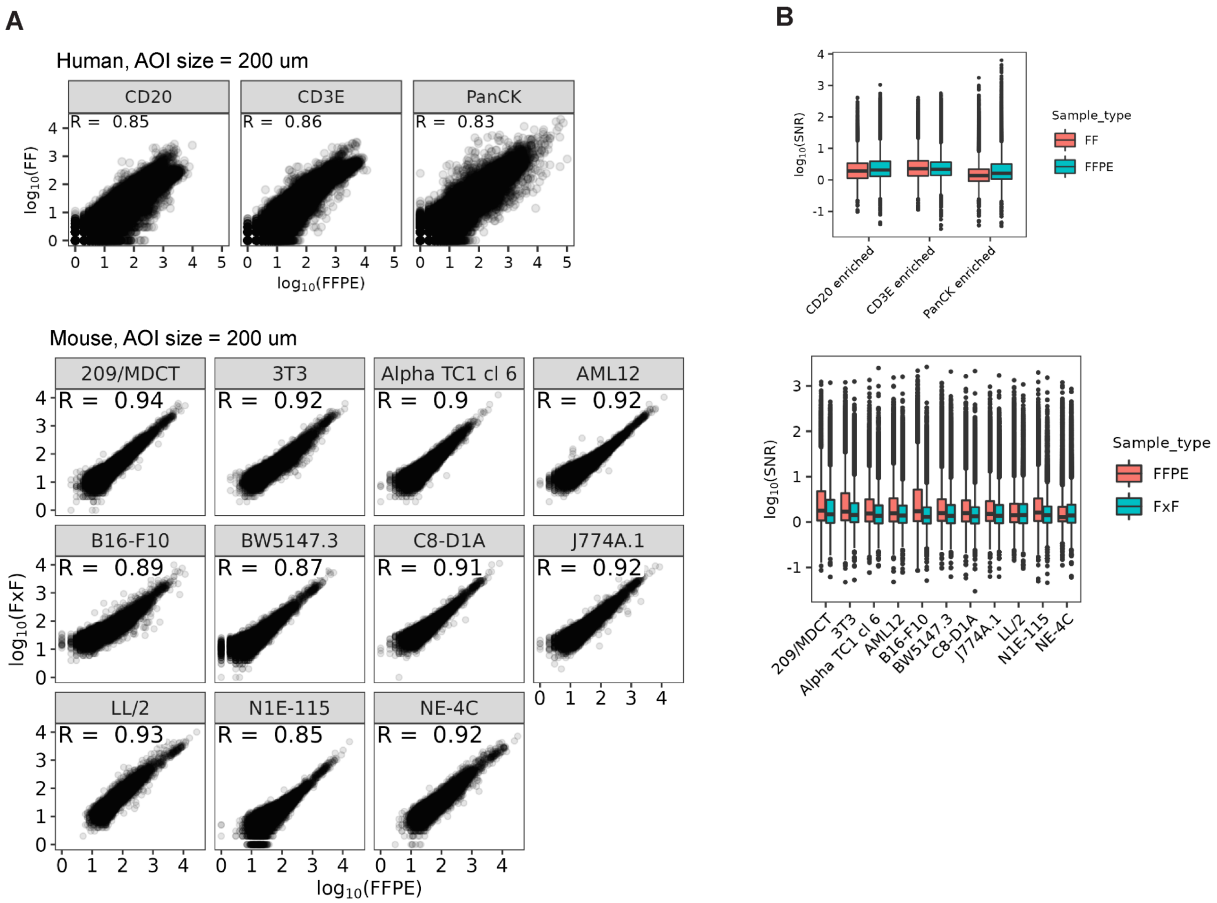

Figure S6. WTA is compatible with human fresh-frozen and mouse fixed-frozen samples. **A.** Scatterplots of WTA counts for matched CD20- CD3E- and PanCK-enriched regions in FFPE vs fresh frozen (FF) tonsil tissue (human, top) and FFPE vs fixed-frozen (FxF) cell pellets (mouse, bottom). Pearson correlation coefficients are indicated on each plot. **B.** Comparison of signal-to-background ratio of all genes in FFPE vs FF tonsil tissue (human, top) and FFPE vs FxF cell pellets (mouse, bottom).

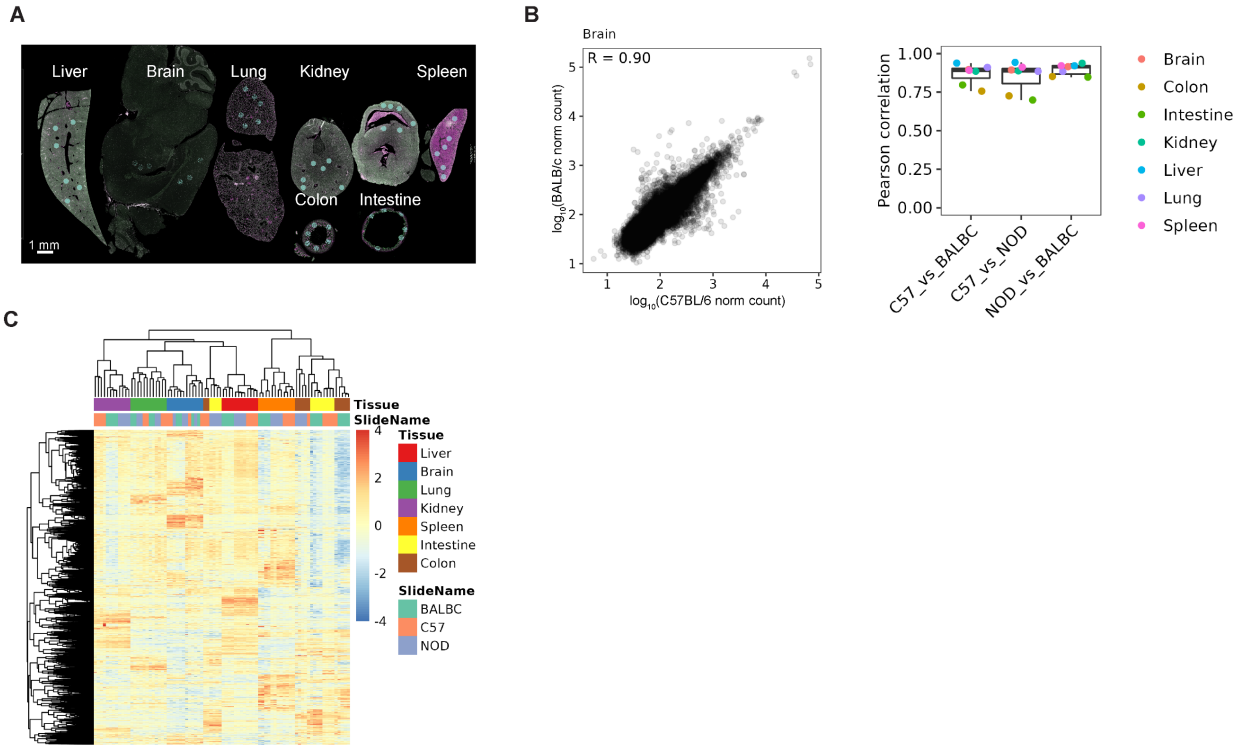

Figure S7. Mouse WTA is compatible with commonly used mouse strains. A. Image of the C57BL/6 FFPE organ array used in this experiment, with the 7 tested organs labeled. Similar tissue arrays from two other mouse strains (BALB/c, NOD) were also profiled. **B.** Left: Representative scatterplot of WTA counts in the brain between C57BL/6 and BALB/c. Right: Boxplot of correlation coefficients of all comparisons between strains for each organ. **C.** Heatmap of scaled gene expression of the 16,610 genes expressed above background in at least 10% of AOIs. AOIs and genes are clustered by hierarchical clustering.

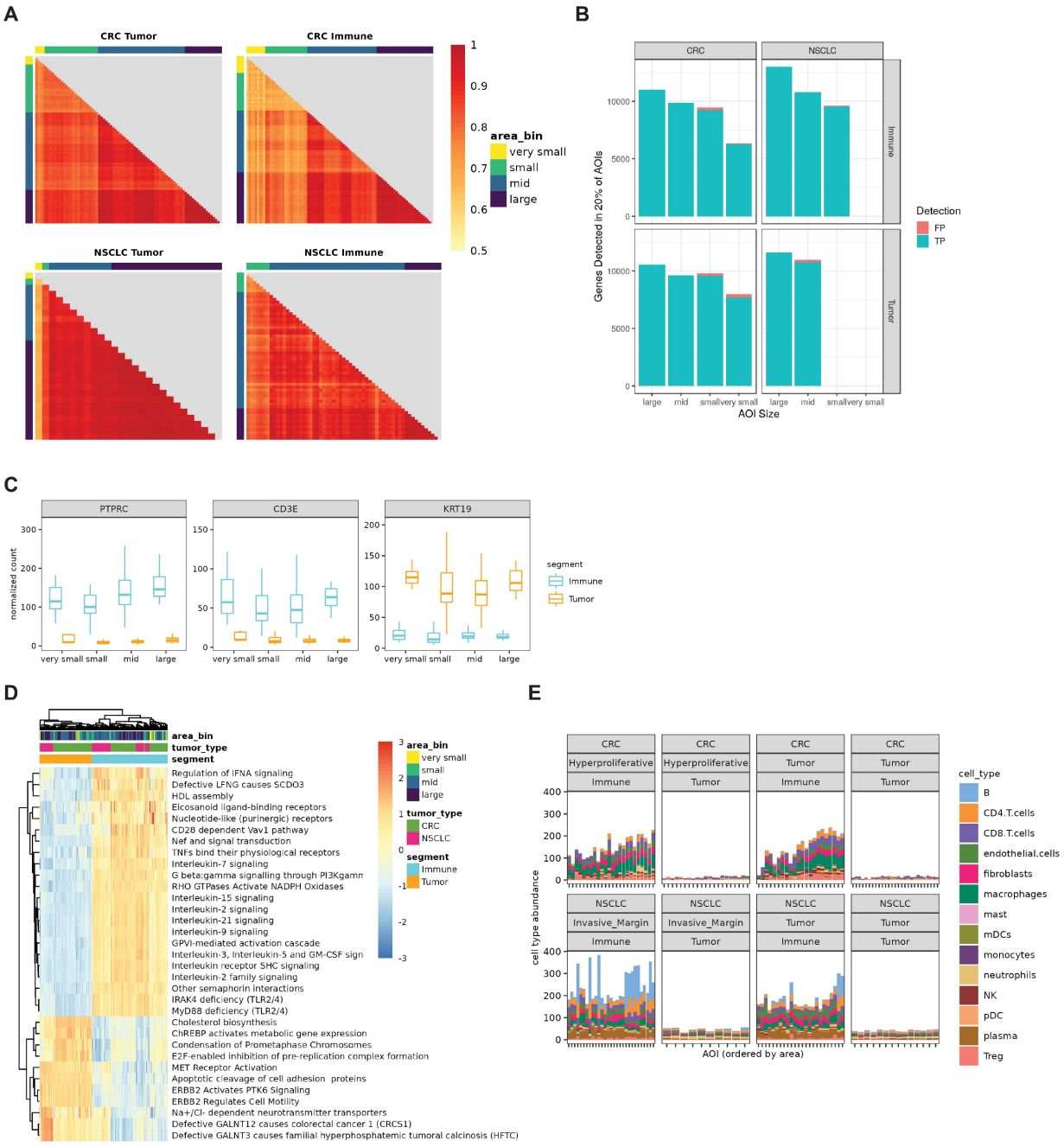

Figure S8. Correlation of WTA counts, detected genes, pathway analysis, and cell type deconvolution results across AOI sizes in CRC and NSCLC. A. Pearson's correlation of counts from all genes from each AOI to every other AOI of the same tumor and segmentation type. AOIs are ordered by area. **B.** Number of genes detected in at least 20% of AOIs in each

size bin that are also detected in the “large” size bin. Shared genes are in blue, unique genes are in red. **C.** Boxplots showing Q3 normalized count of genes encoding CD3E, PTPRC, and KRT19, which were used as morphology markers for the segmentation. **D.** Heatmap of ssGSEA enrichment of the most differentially expressed Reactome pathways between tumor and immune compartments. Enrichment was computed using genes detected above background in >20% of AOIs. Columns and rows are clustered by hierarchical clustering and annotated by tumor type, segment, and area bin. All displayed pathways are significant at FDR < 0.01. **E.** Results of cell type deconvolution using a cell profile matrix derived from gene expression profiles of tumor, stroma, and immune cells (Danaher et al.). Data are shown as stacked barplots with each bar as a single AOI, and the estimated abundance of each immune cell type colored and faceted by tumor type, segment, and region within the tumor.

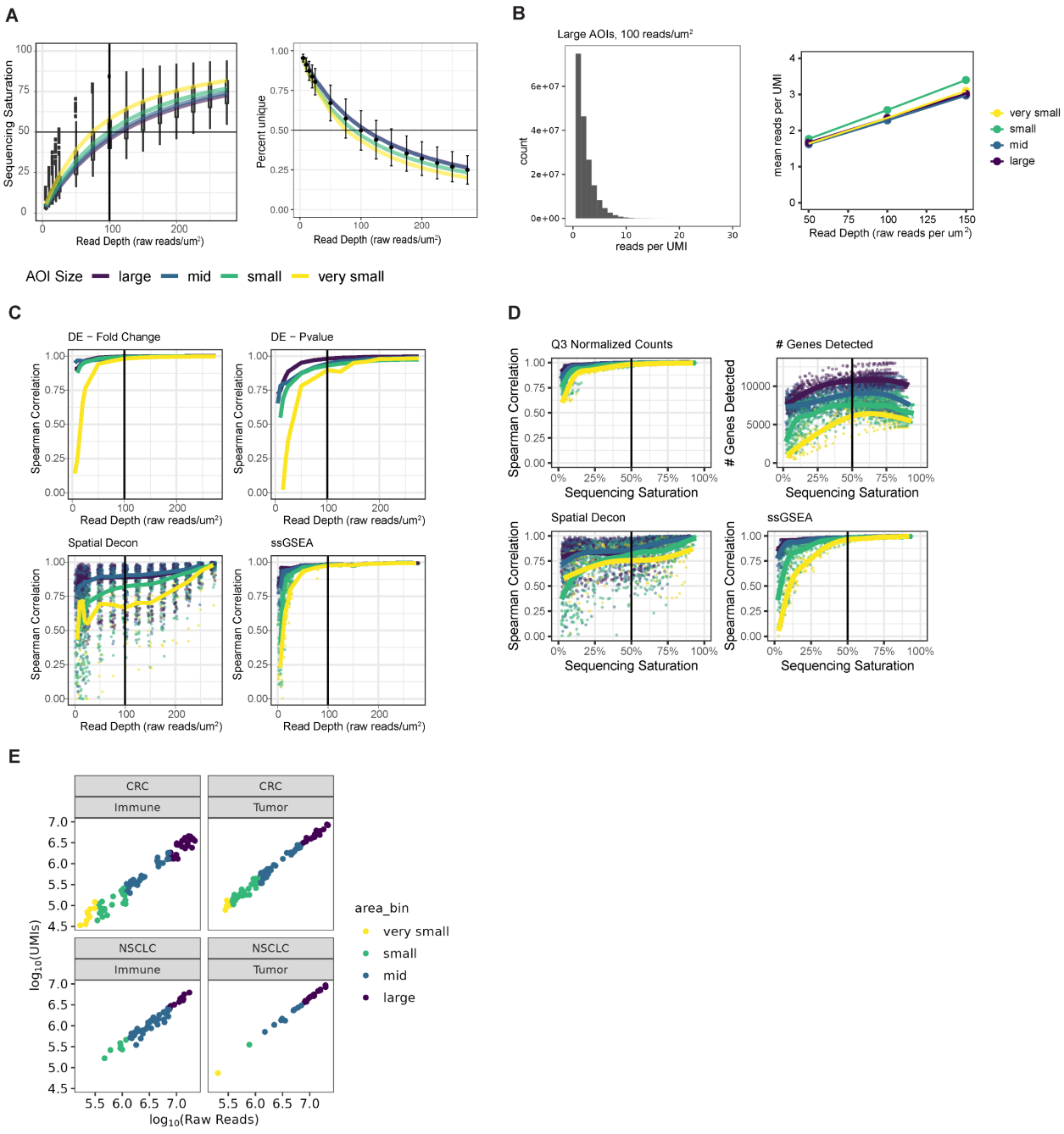

Figure S9. Effect of read depth on performance metrics and biological analyses of human WTA. A. Relationship between read depth (raw reads/μm^2) and sequencing saturation (1-deduplicated/aligned) (left) or percent unique reads (right) split by AOI size. **B.** Relationship between read depth and number of reads per UMI. Example histogram of reads per UMI for large AOIs subsampled to 100 raw reads/μm^2 (left), and mean reads per UMI for all size bins at 50,

100, and 150 raw reads/μm^2 (right). **C.** The first panel shows genes detected above background per AOI at each size and subsampling level. The other panels show Spearman's correlation of counts, results from cell type deconvolution, differential expression fold change and p-value, and ssGSEA enrichment in subset AOIs to the same AOI at 300 raw reads/μm^2. Jittered points are individual AOIs and lines represent the average for each AOI size, colored by area bin. Differential expression (DE) does not have individual AOI points since it is run by segment group (Tumor vs Immune) rather than by AOI. AOI sizes are colored as in A. **D.** Same calculations as B but plotted against individual AOI's sequencing saturation instead of read depth. **E.** Scatterplots showing $\log_{10}$ counts of raw reads versus $\log_{10}$ UMI deduplicated counts for each AOI. Data is shown for the 150 reads/μm^2 subsampling level.

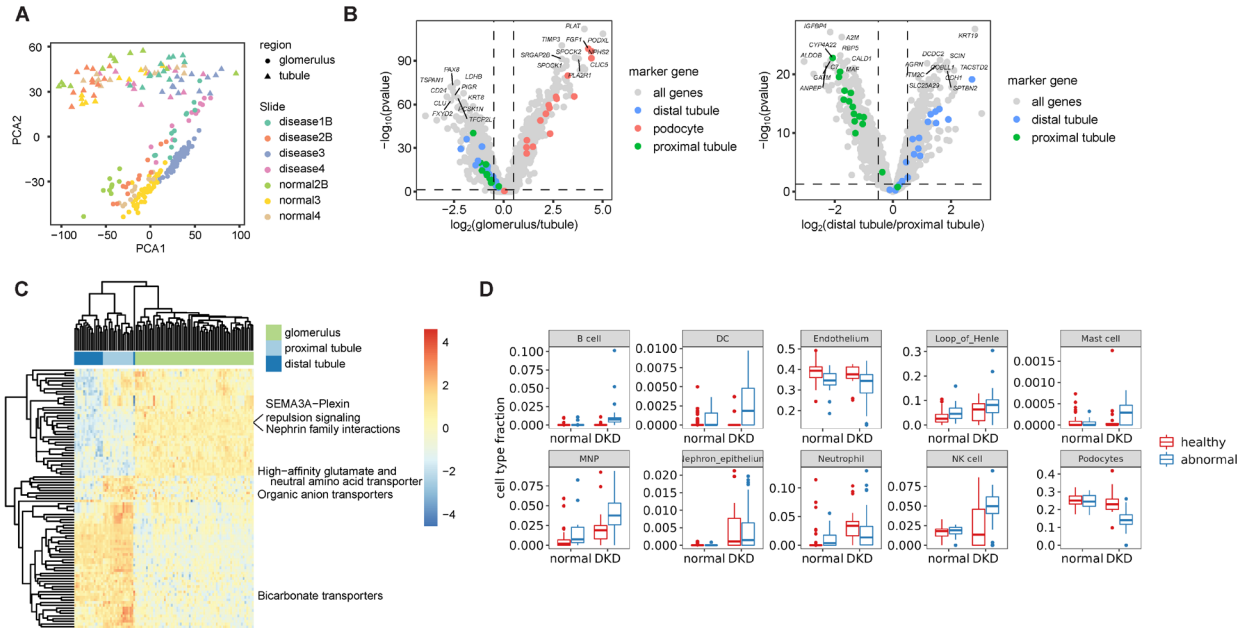

Figure S10. Additional analyses of the human kidney dataset. A. Principal component analysis of variation between samples using genes detected above background in >1% of AOIs. PCA1 vs PCA2 is plotted, with points colored by sample and shaped by kidney structure. **B.** Volcano plots of fold change vs -$\log_{10}$(*p*-value) from differential expression analysis of normal glomeruli vs tubules, and proximal tubules vs distal tubules. Top marker genes identified in

proximal tubule cells, distal tubule cells, and podocytes from published scRNA-seq data (Young et al. 2018) are colored. **C.** Heatmap of ssGSEA enrichment of the most differentially expressed Reactome pathways between substructures in normal kidney samples. Enrichment was computed using genes detected above background in >1% of AOIs. Columns and rows are clustered by hierarchical clustering and the data are scaled by row. All displayed pathways are significant at FDR < 0.05. **D.** Boxplots of all cell types with significantly different proportions between normal and DKD glomeruli (*t*-test Bonferroni-corrected *p*-value < 0.05), colored by pathological annotation.

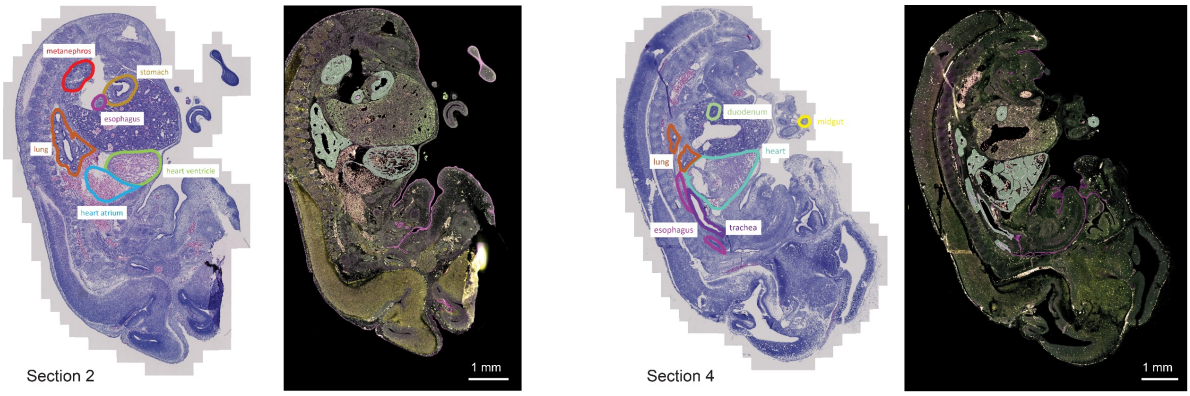

Figure S11. Annotation of mouse embryo organs. DSP fluorescent images (right) and H&E images of serial sections (left) of two representative sections of the mouse embryo. Organs profiled are outlined and labeled.